THE JOURNAL OF PHYSICAL CHEMISTRY C

Article

pubs.acs.org/JPCC

Covalent Immobilization of $Cu_3(btc)_2$ at Chitosan–Electroreduced Graphene Oxide Hybrid Film and Its Application for Simultaneous Detection of Dihydroxybenzene Isomers

Yizhen Yang, Qingxiang Wang,* Weiwei Qiu, Hongxu Guo, and Feng Gao

College of Chemistry and Environment, Fujian Province Key Laboratory of Modern Analytical Science and Separation Technology, Minnan Normal University, Zhangzhou 363000, P. R. China

Supporting Information

ABSTRACT: The metal–organic framework (MOF) of $Cu_3(btc)_2$ (btc = benzene-1,3,5-tricarboxylic acid) is covalently immobilized at chitosan (CS)–electrochemically reduced graphene oxide (ERGO) hybrid film modified electrode, which is characterized by scanning electron microscope (SEM), energy-dispersive X-ray spectra (EDS), and electrochemistry. The MOF-based electrode is applied as an electrochemical sensing platform for the simultaneous detection of dihydroxybenzene isomers (DBIs) of catechol (CT), resorcinol (RS), and hydroquinone (HQ). The results show that the DBIs present well-resolved and intense voltammetric signals at the modified electrode, due to the synergic effect contributing from $Cu_3(btc)_2$ with unique porous framework structure and ERGO with high electronic conductivity. The excellent distinguishing efficiency of the sensor toward DBIs is also confirmed by the quantum chemical computation. Quantitative analysis assays by differential pulse voltammetry shows that the sensor has wide linear ranges and low detection limits for the DBIs. The developed sensor is also applied for the determination of DBIs in the real water sample, and satisfactory results are obtained. This work strongly implies that the MOFs have great potential in the construction of novel electrochemical sensor for isomers.

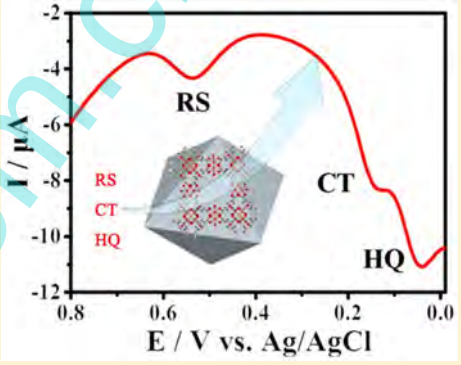

1. INTRODUCTION

Catechol (CT), resorcinol (RS), and hydroquinone (HQ) are three typical dihydroxybenzene isomers (DBIs) of phenolic compounds, which usually coexist in environmental samples as pollutants.[1] Due to their high toxicity and low degradability in the ecological environment, it is necessary to develop simple and rapid analytical technology for the determination of them. To date, several analytical methods have been established to quantitatively determine DBIs, such as high-performance liquid chromatography,[2] fluorescence,[3] chemiluminescence,[4] spectrophotometry,[5] mass spectrometry,[6] capillary electrochromatography,[7] and electrochemical methods.[8,9] Among them, the electrochemical methods attract considerable attention due to their advantages of fast response, low cost, high sensitivity, and excellent selectivity. However, because the three isomers of CT, RS, and HQ have similar stereochemical structure and close redox potentials on common electrode, the simultaneous determination of them is usually hardly achieved. In order to overcome this drawback, some functional materials such as carbon nanotubes,[10] metal sulfides,[11] quantum dots,[12] graphene,[13] etc. have been utilized as the electrochemical sensing materials for simultaneous determination of them. However, these materials suffer the defects of complicated synthesis process, high toxicity, and/or poor analytical performance. Therefore, it is still a challenge to develop robust and convenient sensing platform for the simultaneous determination of DBIs.

Metal–organic frameworks (MOFs) are a type of novel three-dimensional (3D) coordination compounds with the features of controllable synthesis, structural diversity, porosity, high specific surface areas, rich active site, and high flexibility of the pore size. On the basis of these, the MOFs receive increasing attention in the application of gas separation,[14] gas storage,[15] catalysis,[16] and chromatographic purification[17] in the past decade. Recently, the application of MOFs in electrochemical energy areas including fuel cells,[18] supercapacitors,[19] solar cells,[20] rechargeable lithium batteries[21] also gets significant interest owing to their good electrochemical performance. Besides, the MOFs have also been regarded as a promising candidate for constructing electrochemical sensors due to the following reasons: (1) The high porosity and large surface area are helpful to concentrate the analytes at the higher level, which can produce stronger signal intensity as well as higher sensitivity. (2) Tunable pore size and topologic structure allow the MOFs-based matrix having good selectivity to capture the target analytes with appropriate size and configuration; (3) The analyte molecules can interact with MOFs through

Received: February 16, 2016
Revised: April 28, 2016
Published: April 28, 2016

DOI: 10.1021/acs.jpcc.6b01574
J. Phys. Chem. C 2016, 120, 9794–9803

Scheme 1. Illustration of the Construction and Detection Strategy of the Sensor

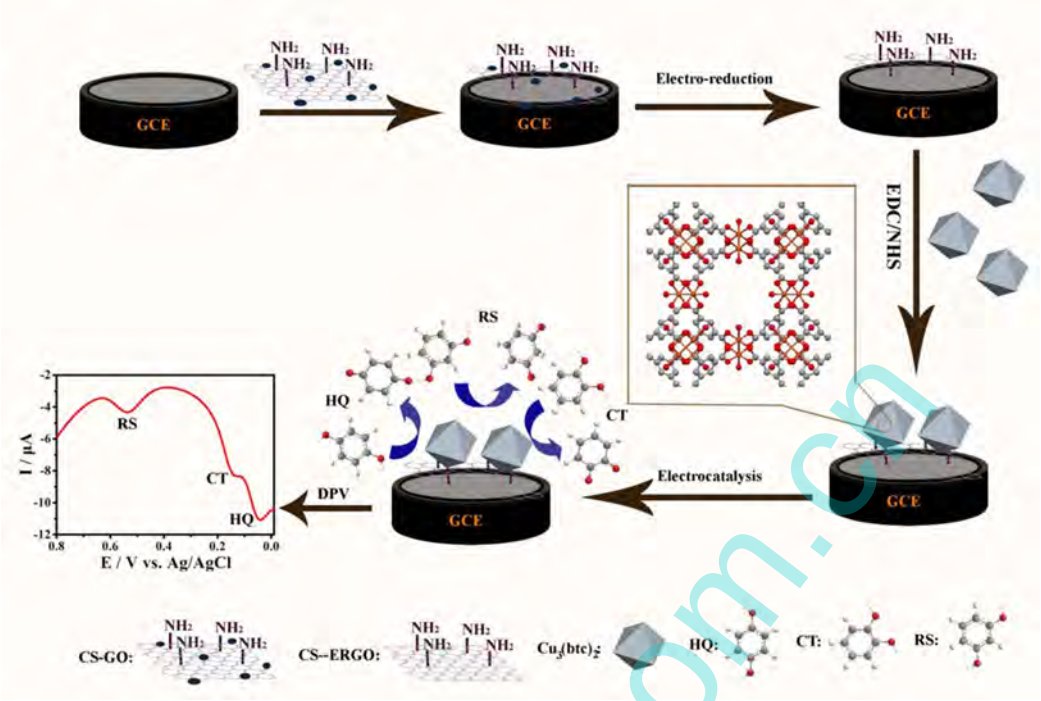

reversible physical adsorption, which makes the sensors have superior regenerative ability and fast response kinetics. Inspired by these expected merits, increasing amounts of MOFs-based electrochemical sensors have been reported in recent years for the detection of various analytes including DNA,[22] hydrogen peroxide,[23] ascorbic acid,[24] and dopamine and acetaminophen.[25]

$Cu_3(btc)_2$ (btc = benzene-1,3,5-tricarboxylic acid), one of the first MOF compounds, has an intersecting 3D network containing large pores with a square cross section.[26] In the past decade, the $Cu_3(btc)_2$ MOF has been studied extensively in the fields of gas sorption, storage, and separation.[26] In recent years, the application potential of the MOF material in electroanalytical field has also been continually exploited. For example, it has been utilized as the electrochemical sensing material for the detection of glucose,[27] lead,[28] and H_2O_2/ascorbic acid.[29] Nevertheless, to the best of our knowledge, we have not found the application of $Cu_3(btc)_2$ as an electrochemical sensing material for the highly selective and sensitive detection of isomers.

Herein, we fabricated a novel electrochemical sensing platform for the detection of DBIs through covalent immobilization of the electroactive $Cu_3(btc)_2$ MOF on a functional matrix of chitosan (CS)−electrochemically reduced graphene oxide (ERGO) (Scheme 1). Chitosan (CS) is an interesting polysaccharide biopolymer that has been widely used in the fields of agriculture, horticulture, industry, biomedicine, and chemical sensors, owing to its numerous advantages like nontoxic nature, excellent film-forming ability, rich active groups, high permeability, and cost-effectiveness.[30,31] On the basis of these advantages, CS was coated on the electrode surface during fabrication of the sensing interface in this work and then used as the supporting carrier for the grafting of $Cu_3(btc)_2$. The good film-forming ability and the stable covalent binding endow the sensing surface with a high stability. On the other hand, in order to improve the electronic conductivity of the electrode, the graphene oxide (GO) was doped with CS and then transformed to the highly electroconductive reduction form through a simple eletroreduction method.[25] The morphology and structure of the obtained materials and sensing interface were characterized using scanning electron microscopy (SEM), atomic force microscopy (AFM), and energy-dispersive X-ray spectroscopy (EDS). The electrochemical experiments show that based on the unique porous nature and inherent redox-activity of $Cu_3(btc)_2$, the DBIs of RS, CT, HQ can be well separated from each other. Meanwhile, the high conductivity of the CS−ERGO matrix greatly enhances the electrochemical signal intensity of the DBIs, leading to a high sensitivity of the sensor with the detection limit of 0.44 μM, 0.41 μM, and 0.33 μM for HQ, CT, and RS, respectively. Also the accurate determination of DBIs in the real samples is realized by the proposed sensor, which broadens the application of the MOF materials in the analytical fields.

2. EXPERIMENTAL SECTION

2.1. Reagents and Apparatus. HQ, CT, RS, 1-ethyl-3-(3-dimethylaminopropyl)carbodiimide (EDC), and *N*-hydrosulfosuccinimide (NHS) were purchased from Sigma-Aldrich Co., Ltd. (China). Benzene-1,3,5-tricarboxylic acid (btc) and chitosan (CS) were purchased from Aladdin Reagent Co., Ltd. (China). Copper nitrate trihydrate ($Cu(NO_3)_2{\cdot}3H_2O$) was obtained from Xilong Chemical Co., Ltd. (China). 25 mM phosphate buffered solution (PBS, pH 7.0) was purchased from Shanghai KangYi Instruments Co., Ltd. (China). All the other chemicals were of analytical reagent and used without further purification. All aqueous solutions were prepared by deionized water.

AFM measurements were carried out on CSPM5500 (China). Fourier transform infrared (FT-IR) spectroscopy was performed on a Nicolet iS 10 spectrometer (USA). To prepare pellets, the samples were first dried at 358 K for 5 h and

DOI: 10.1021/acs.jpcc.6b01574
J. Phys. Chem. C 2016, 120, 9794−9803

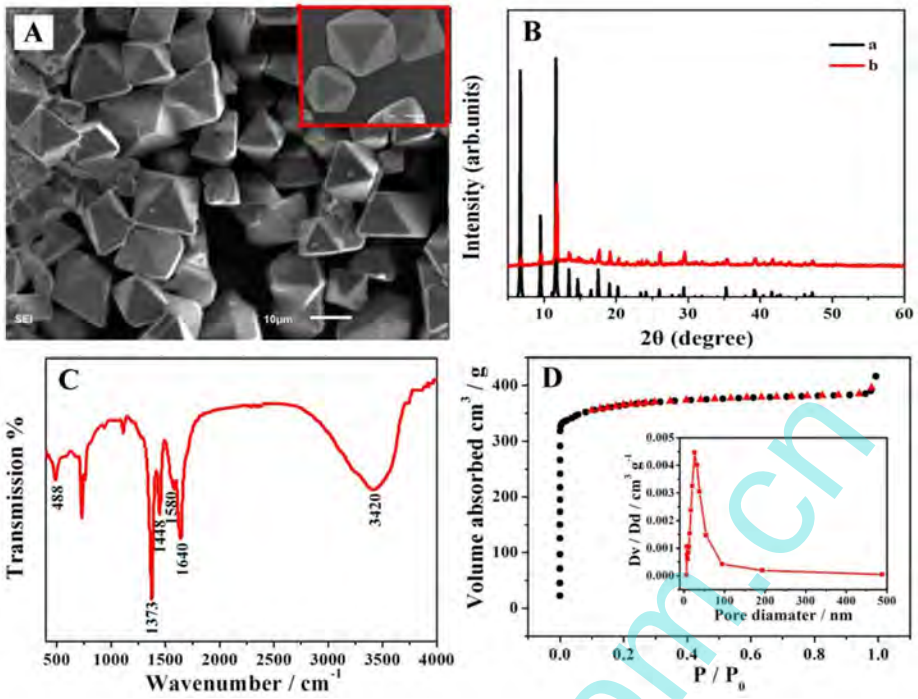

Figure 1. Low magnification (main panel) and high magnification (inset) SEM images (A), the standard (CSD: XAMDUM06) (a) and experimental (b) XRD pattern (B), FT-IR spectrum (C), nitrogen adsorption−desorption isotherm curve (main panel), and its pore size distribution curve (inset) (D) of the $Cu_3(btc)_2$ synthesized.

then mixed with KBr at a mass ratio of 1:100, ground to powder in an agate. A hydraulic press was used to press the mixtures to disks of 5 mm in diameter at 10 MPa for 3 min. The spectrum was collected in the 400−4000 cm^{-1} wavenumber range at a resolution of 4 cm^{-1}. SEM and EDS were recorded on a JEOL JMS-6010LA field emission scanning electron microscope (Japan). The crystal structure was analyzed by X-ray powder diffraction (XRD) on a Rigaku D/MAX-RB diffractometer (Japan). The surface area and pore size distribution of material were measured by Brunauer−Emmett−Teller (BET) and Barrett−Joyner−Halenda (BJH) procedures on Belsorp-MAX (USA). Electrochemical experiments were tested on CHI 6043E electrochemical analyzer (China) in connection with a three-electrode system using a modified glassy carbon electrode (GCE, Φ = 3 mm) as the working electrode, platinum electrode as the counter electrode, and Ag/AgCl (3 M KCl) electrode as the reference electrode.

2.2. Preparation of GO−CS Dispersion and $Cu_3(btc)_2$ MOF Material. First, the graphene oxide (GO) was prepared according to the modified Hummer's method.[32] In brief, graphite (1 g) was mixed with concentrated sulfuric acid (46 mL) in a 200 mL flask. The mixture was stirred for 2 h in an ice bath, and then sodium nitrate (1 g) was added and a constant temperature (3 °C) was kept for 30 min. After that, potassium permanganate (6 g) was slowly added into the mixture and the temperature was controlled to be lower than 20 °C. The ice bath was then removed, and the mixture was heated to 38 °C and maintained for 2.5 h, followed by adding 50 mL of deionized water and reacting at 98 °C for 30 min. Finally, H_2O_2 (12.5 mL, 30%) and deionized water (50 mL) were added into the mixture to terminate the reaction. For purification, the product was washed with 3% HCl and deionized water several times and dried at 60 °C in oven. The GO−CS composite was prepared by adding 100 μL of 1.0% acetic acid solution containing 0.3 wt % CS into 100 μL of 1 mg mL^{-1} aqueous GO, and then the mixture was ultrasonicated for 15 min under 100 W to obtain a homogeneous dispersion.

The MOF of $Cu_3(btc)_2$ was prepared by a solvothermal method according to the previous literature.[33] Typically, $Cu(NO_3)_2{\cdot}3H_2O$ (0.545 g) dissolved in deionized water (7.5 mL) was mixed with ethanol (7.5 mL) containing btc (0.264 g). After ultrasonication for 15 min, the mixture was placed into a Teflon-lined stainless steel reactor and heated at 120 °C for 24 h. The blue solid was collected by centrifugation and washed with ethanol and deionized water. Subsequently, the blue precipitates were dried at 80 °C for 10 h in vacuum.

2.3. Fabrication of the Modified Electrodes. The bare GCE was polished carefully with alumina slurry of 1.0, 0.3, and 0.05 μm in turn and then cleaned by ultrasonic washing in ethanol and deionized water, respectively. After the cleaned GCE was dried by N_2 flow, 10 μL of CS−GO was cast onto the electrode surface. Upon dryness under room temperature, the GO in the composite film of CS−GO was electrochemically reduced by cyclic scan between −1.6 and 0.6 V in 25 mM PBS (pH 7.0) until constant curves were achieved. Afterward, the obtained electrode was incubated in 2 mg mL^{-1} $Cu_3(btc)_2$ homogeneous suspension that was premixed with PBS containing 10 mM EDC and 20 mM NHS for 2 h. Finally, the modified electrode was carefully rinsed with deionized water to remove loosely attached $Cu_3(btc)_2$. Thus, the $Cu_3(btc)_2$ modified electrode was obtained, which was denoted as $Cu_3(btc)_2$/CS−ERGO/GCE. For comparison, the modified electrodes of CS−ERGO/GCE and $Cu_3(btc)_2$/CS−GO/GCE were prepared in the same way.

2.4. Quantum Chemical Computation. The quantum chemical computation was carried out with the Guassian 09 package and simulation package (NWChem):[34,35] In brief, all the molecular orbital calculations on DBIs were carried out

DOI: 10.1021/acs.jpcc.6b01574
J. Phys. Chem. C 2016, 120, 9794−9803

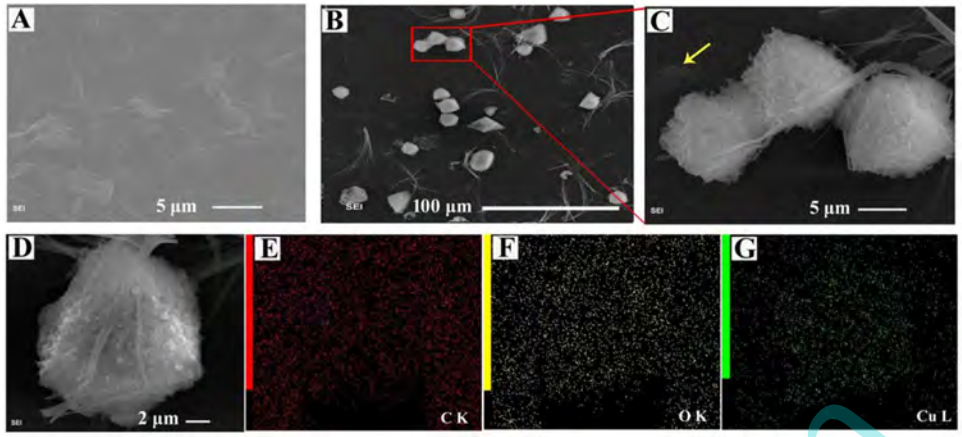

Figure 2. SEM images of CS−ERGO/GCE (A), $Cu_3(btc)_2$/CS−ERGO/GCE with low (B) and high resolution (C), SEM (D), and EDS elemental mapping analysis of a single $Cu_3(btc)_2$ particle (E−G).

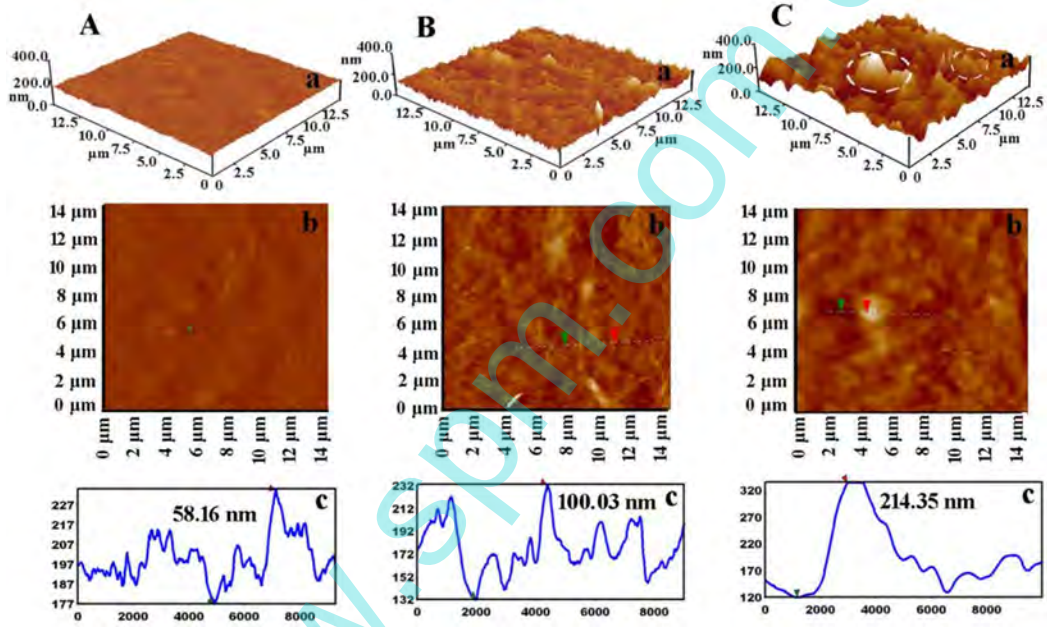

Figure 3. Topographic (a), three-dimensional (b), and cross-sectional (c) AFM images of CS/GCE (A), CS−ERGO/GCE (B), and $Cu_3(btc)_2$/CS−ERGO/GCE (C).

with the Guassian 09 package using the density functional theory (DFT)/6-31G++** method. The molecular orbital calculation on the $Cu_3(BTC)_2$ MOF was achieved with an open source simulation package (NWChem)[36] using the spin-unrestricted DFT formalism with the B3LYP exchange−correlation functional (UB3LYP)[37] and the Ahlrich triple-ζ valence basis set with polarization on all atoms (TZVP).[38]

3. RESULTS AND DISCUSSION

3.1. Morphology and Structure Characterization of $Cu_3(btc)_2$ MOF. Figure 1A shows the SEM image of the synthesized $Cu_3(btc)_2$ particles, in which a large amount of particles with well-defined octahedral morphology is observed. From the high-magnification image (inset of Figure 1A), it can be seen that the $Cu_3(btc)_2$ particle has the edges length of about 14 μm and an opposite-vertical-apex length of about 18 μm. Additionally, the particles show sharp edge and smooth surface, suggesting that the as-synthesized sample has good crystallinity and high purity. The XRD result (curve b in Figure 1B) shows that all the diffraction peaks of the sample are well indexed to the face-centered cubic phase of stimulated standard card (CSD: XAMDUM06, curve a in Figure 1B), testifying that the $Cu_3(btc)_2$ has been successfully synthesized.

The structure of $Cu_3(btc)_2$ was provided by FT-IR spectroscopy as shown in Figure 1C. The characteristic peak centered at 488 cm^{-1} can be assigned to the Cu−O bond. The absorption bands of 1640 and 1580 cm^{-1}, and 1448 and 1373 cm^{-1} are assigned to the asymmetric and symmetric stretching vibrations of the carboxylate groups in btc linker,[39] respectively. In order to investigate the textural properties such as surface area and pore volume of the synthesized MOF, the BET surface area and pore volume measurements of the sample were measured by nitrogen adsorption−desorption isotherms. Figure 1D shows the typical N_2 adsorption−desorption isotherms at 77 K and the Barrett−Joyner−Halenda (BJH) desorption pore size distribution of the synthesized $Cu_3(btc)_2$. From the results, it can be seen that the isotherm is a typical I type curve, confirming the presence of the microporous structure of the

DOI: 10.1021/acs.jpcc.6b01574
J. Phys. Chem. C 2016, 120, 9794−9803

MOF. According to the corresponding pore size distribution curve (inset of Figure 1D), the pore size was measured to be 33.7 Å. The BET surface area of $Cu_3(btc)_2$ was determined to be 1324.6 $m^2 g^{-1}$. Such a high surface and pore size are helpful for the synthesized MOF to concentrate large amount of analytes for the sensing application.

3.2. SEM and AFM Characterization on the Fabrication of $Cu_3(btc)_2$ Modified Electrode. The immobilization of $Cu_3(btc)_2$ at CS−ERGO modified electrode (CS−ERGO/GCE) was characterized by SEM and AFM. Figure 2 displays the SEM images of CS−ERGO/GCE upon modification with preactivated $Cu_3(btc)_2$. The results show that the CS−ERGO/GCE presented some obvious crumpled and scrolling layers (Figure 2A), which suggested that the graphene material has been successfully attached on the electrode surface. Interestingly, after the CS−ERGO/GCE was reacted with $Cu_3(btc)_2$ that was preactivated by EDC/NHS, some solid particles were found to distribute on the surface of CS−ERGO/GCE (Figure 2B). The higher magnification image of the particles revealed that the immobilized $Cu_3(btc)_2$ still has the basic octahedral shape of the pristine $Cu_3(btc)_2$ particles, but the surface of the particle becomes very coarse (Figure 2C), which might be caused by the aggregation of microcrystals on the surface of $Cu_3(btc)_2$ during the activation process.[40] EDS elemental mapping analysis indicates the presence of Cu, C, and O components in the hybrid (Figure 2E−G), which is the clear evidence for the successful immobilization of $Cu_3(btc)_2$ on CS−ERGO/GCE.

Atomic force microscopy (AFM) is a high-resolution scanning probe microscopy, which can be conducted to probe the topography changes of an interface. Figure 3 shows the three-dimension (3D) (curve a), topographic (curve b), and cross-sectional (curve c) AFM images of CS/GCE (A), CS−ERGO/GCE (B), and $Cu_3(btc)_2$/CS−ERGO/GCE (C). As seen, the surface of CS/GCE is relatively flat and smooth with the largest height of 58.16 nm. The value of the roughness calculated from different regions is 8.44 nm. But for CS−ERGO/GCE, it is observed that lots of adjacent peaks appeared. The largest peak height and the roughness are increased to 100.03 and 11.8 nm, respectively, suggesting that the ERGO nanomaterial has been entrapped within the CS film and enhanced the surface area of the modified electrode. When CS−ERGO/GCE was grafted with $Cu_3(btc)_2$, it is found that the morphology of the electrode becomes more rough, and many hills stretching over several micrometers (see the circles in the figure) are visible. The height and the average roughness are extremely increased to 214.35 and 20.8 nm, respectively. These changes also indicate that the $Cu_3(btc)_2$ has been anchored on CS−ERGO/GCE by the proposed method.

3.3. Electrochemical Behavior of $Cu_3(btc)_2$/CS−ERGO/GCE. The electrochemical properties of the different modified electrodes were evaluated via cyclic voltammetry (CV). Figure 4 shows the CVs of CS−GO/GCE (curve a), CS−ERGO/GCE (curve b), $Cu_3(btc)_2$/CS−GO/GCE (curve c), and $Cu_3(btc)_2$/CS−ERGO/GCE (curve d) in 25 mM PBS (pH 7.0). It is found that there is no Faradaic response for CS−GO/GCE at the high potential range from −0.4 to 0.8 V, but a small and irreversible peak ascribed to the reduction of the dissolved oxygen occurs at the low potential of −0.55 V (Figure S1 in Supporting Information). After electroreduction treatment of electrode, the background current of the CV curve increases obviously, and meanwhile the reduction peak of the dissolved oxygen enlarges and negatively shifts obviously. This indicates

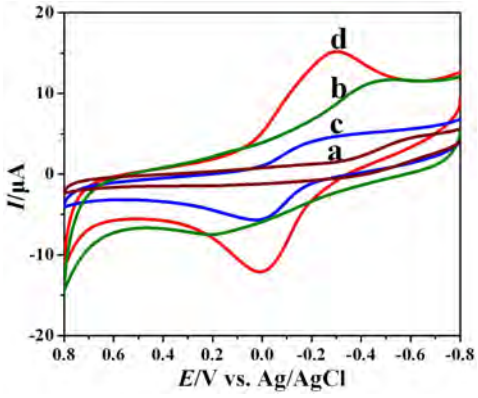

Figure 4. CVs of CS−GO/GCE (a), CS−ERGO/GCE (b), $Cu_3(btc)_2$/CS−GO/GCE (c), and $Cu_3(btc)_2$/CS−ERGO/GCE (d) in 25 mM PBS (pH 7.0). Scan rate: 0.1 V s^{-1}.

that the GO on the electrode has been successfully reduced, resulting in the improvement of the effective surface area and electron-transfer kinetics of the electrode interface. Such an enhancement effect is further proved by the different electrochemical response of these two electrodes after grafting with $Cu_3(btc)_2$. For $Cu_3(btc)_2$/CS−GO/GCE, it is observed that a pair of small redox peaks at the high potentials of 0.001 V and −0.274 V are newly appeared (curve c). According to the literature,[41] the Faradaic signal can be assigned to redox process of Cu^{II}/Cu^{I} couple from $Cu_3(btc)_2$. The ratio of oxidation peak current (I_{pa}) to reduction peak current (I_{pc}) was determined to be 1.93, which is quite far away from 1 unit, suggesting that the electrochemical process of $Cu_3(btc)_2$ at CS−GO/GCE has poor reversibility. In contrast, the redox peak currents obtained at $Cu_3(btc)_2$/CS−ERGO/GCE (curve d) increases obviously in comparison with $Cu_3(btc)_2$/CS−GO/GCE and the value of I_{pa}/I_{pc} (=0.97) was changed to about 1 unit, demonstrating that the electrochemical reversibility of $Cu_3(btc)_2$ on CS−ERGO is dramatically changed. All these experiments indicate that an electroactive interface with high electrochemical activity is achieved through the facile covalent immobilization of $Cu_3(btc)_2$ MOF on the functional matrix of CS−ERGO hybrid film.

3.4. Electrochemical and Quantum Chemical Calculation on the Distinguishing of $Cu_3(btc)_2$/CS−ERGO/GCE toward DBIs. In order to probe the potential application of $Cu_3(btc)_2$/CS−ERGO/GCE, the modified electrode was utilized for the simultaneous detection of DBIs including RS, CT, and HQ. Figure 5A depicts the CVs of 25 mM PBS (pH 7.0) in the presence of 0.1 mM HQ (curve a), CT (curve b), or RS (curve c) at $Cu_3(btc)_2$/CS−ERGO/GCE. As seen, all the CVs have a pair of redox peaks at around 0 V and −0.3 V. According to the result of Figure 4, the redox peaks can be assigned to the electron transfer of Cu(II)/Cu(I) couple of the immobilized $Cu_3(btc)_2$, showing that the modified electrode of $Cu_3(btc)_2$/CS−ERGO/GCE remains its original electrochemical characteristic in the presence of the DBIs. When HQ, CT, and RS are separately present in the PBS solution, the new redox peaks at 0.100 V, 0.006 V (for HQ, curve a) and at 0.203 V, 0.094 V (for CT, curve b) and an irreversible oxidation at 0.612 V (for RS, curve c) appear, which suggests that all three isomers present good electrochemical responses at $Cu_3(btc)_2$/CS−ERGO/GCE.

Furthermore, in order to investigate the distinguishing capability of $Cu_3(btc)_2$/CS−ERGO/GCE toward DBIs coex-

DOI: 10.1021/acs.jpcc.6b01574
J. Phys. Chem. C 2016, 120, 9794−9803

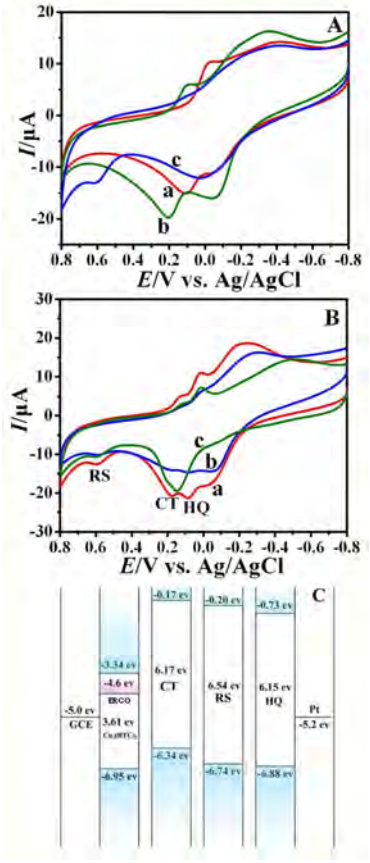

Figure 5. (A) CVs of 25 mM PBS (pH 7.0) with 0.1 mM HQ (a), CT (b), or RS (c) at $Cu_3(btc)_2$/CS−ERGO/GCE. (B) CVs of 0.1 mM HQ, CT, and RS mixture at $Cu_3(btc)_2$/CS−ERGO/GCE (a), $Cu_3(btc)_2$/CS−GO/GCE (b), and CS−ERGO/GCE (c) in 25 mM PBS (pH 7.0). Scan rate: 0.1 V s^{-1}. (C) Flat band model (LUMO and HOMO) of $Cu_3(BTC)_2$, HQ, CT, and RS, and work function for the ERGO and Pt electrodes.

isting in solution, a mixture containing HQ, CT, and RS was prepared and measured with $Cu_3(btc)_2$/CS−ERGO/GCE. The result is displayed as curve a in Figure 5B. As well seen, a distinct oxidation peak at 0.603 V and two pairs of redox peaks at 0.196 V, 0.102 V and 0.094 V, 0.012 V simultaneously appear in the voltammogram (curve a). Through comparison with Figure 5A, these peaks can be well ascribed to the electrochemical response of RS, CT, and HQ. In addition, the peak-to-peak separations (ΔE_p) for the oxidation peaks of the DBIs are larger than those reported in literatures (Table S1 in Supporting Information), which proves the outstanding resolving ability of the sensing film toward the electrochemistry of DBIs. As controls, the electrochemical responses of the DBIs mixture at the other two electrodes of CS−ERGO/GCE and $Cu_3(btc)_2$/CS−GO/GCE were also tested. It is found that at CS−ERGO/GCE, only two oxidation peaks at 0.605 and 0.149 V are observed (curve c). The former can be attributed to the oxidation of RS and the latter to overlap of the oxidation peaks of CT and HQ, which indicates that the voltammetric peaks of DBIs cannot be fully separated by CS−ERGO/GCE. In addition, when $Cu_3(btc)_2$/CS−GO/GCE was applied, it was observed that all the electrochemical responses of the DBIs are visible (curve b), but the signal intensities are dramatically smaller than those at $Cu_3(btc)_2$/CS−ERGO/GCE. Thus, it can be concluded that the film of $Cu_3(btc)_2$/CS−ERGO has the bifunctional effect for the simultaneous detection of DBIs with excellent distinguishing property from the contribution of $Cu_3(btc)_2$ and high sensitivity from the contribution of highly conductive ERGO.

The electrochemical distinguishing performance of $Cu_3(btc)_2$/CS−ERGO toward DBIs was also evidenced by quantum chemical calculation. It is well-known that the oxidation potential is usually governed by electron transfer from the electroactive molecule to the working electrode and hole transfer from the molecules to the Pt electrode.[28] In this work, the Schottky barrier that formed between the sensing film of $Cu_3(btc)_2$/CS−ERGO and the DBIs is the main origin of the oxidation potential. By considering two barriers for the electrons and holes, from a simple flat band model as displayed in Figure 5C, the oxidation potential can be simply determined by the gap between the lowest unoccupied molecular orbital and the highest occupied molecular orbital (LUMO−HOMO)[42] of the DBIs for the two given electrodes (Figure S3 in Supporting Information). From the result, it is obtained that RS has the largest LUMO−HOMO gap (6.54 eV), therefore yielding the largest oxidation potential, which is in agreement with our observations in the electrochemical experiment. Similarly, the LUMO−HOMO gaps of CT and HQ were evaluated to be 6.17 eV and, 6.15 eV, respectively. The close values of the gaps of the two species indicate that they might have adjacent oxidation peaks, but the different adsorption capacities of $Cu_3(btc)_2$ to them cause their various dipole interactions at the electrode interface through charge transfer, which further widens their oxidation potentials.

3.5. Electrochemical Kinetic Parameters of DBIs at $Cu_3(btc)_2$/CS−ERGO/GCE. To understand the charge transfer characteristics of DBIs on $Cu_3(btc)_2$/CS−ERGO/GCE, we respectively recorded CVs of HQ (A), CT (B), and RS (C) on this electrode at various scan rates (ν). From the CVs as displayed in Figure 6, one can observe that with the increase of scan rates, the electrochemical signals of the DBIs enhance gradually. Meanwhile, the redox peak currents (I_{pa}, I_{pc}) of HQ and CT and the irreversible oxidation peak currents (I_{pa}) of RS show good linear relationships with scan rates (up to 0.5 V s^{-1}) obeying the following regression equations:

HQ (inset a of Figure 6A):

$$I_{pa}/\mu A = -81.0461\nu/(V\,s^{-1}) - 5.7729 \quad (r = 0.9960)$$

$$I_{pc}/\mu A = 53.2349\nu/(V\,s^{-1}) + 4.2040 \quad (r = 0.9921)$$

CT (inset a of Figure 6B):

$$I_{pa}/\mu A = -96.0749\nu/(V\,s^{-1}) - 8.5268 \quad (r = 0.9945)$$

$$I_{pc}/\mu A = 41.0143\nu/(V\,s^{-1}) + 1.5600 \quad (r = 0.9921)$$

RS (inset a of Figure 6C):

$$I_{pa}/\mu A = -76.4147\nu/(V\,s^{-1}) - 4.9443 \quad (r = 0.9945)$$

These results indicate that all the electrochemical reactions of DBIs on the modified electrode are adsorption-controlled. Since the redox peak separations for HQ and CT are both higher than 0.20/n V, the electrochemical parameters of electron transfer coefficient (α) and standard electron transfer

DOI: 10.1021/acs.jpcc.6b01574
J. Phys. Chem. C 2016, 120, 9794−9803

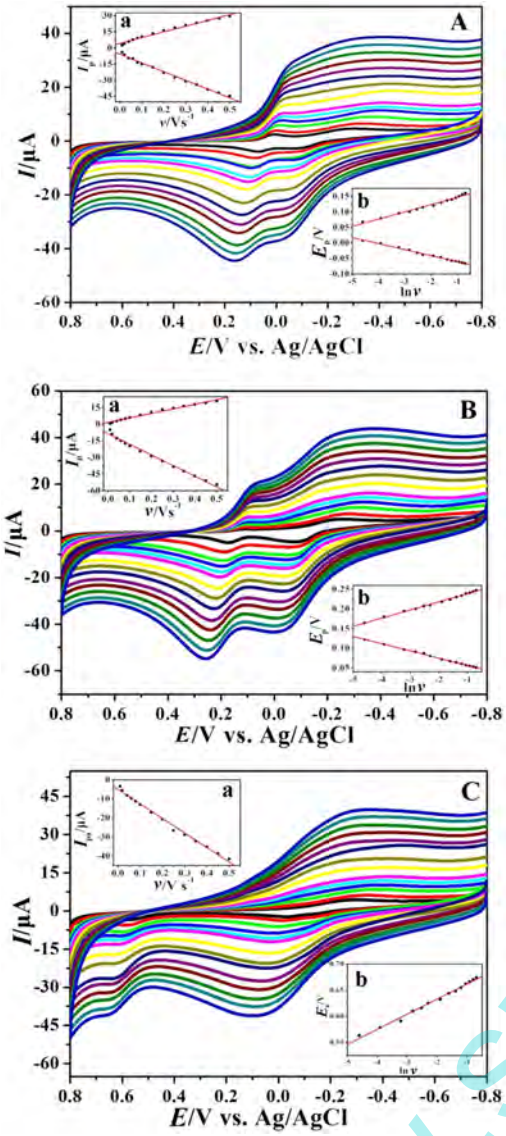

Figure 6. CVs of 0.1 mM HQ (A), CT (B), RS (C) at $Cu_3(btc)_2$/CS−ERGO/GCE at different scan rates from 0.01 V s^{-1} to 0.5 V s^{-1}. Insets a and b show the relationships of peak currents (I_p) versus scan rate (ν) and peak potentials (E_p) versus ln ν.

rate constant (k_s) were then calculated according to following Laviron's eqs 1−3):[43]

$$E_{pc} = E^{0'} - \frac{RT \ln \nu}{\alpha nF} \quad (1)$$

$$E_{pa} = E^{0'} + \frac{RT \ln \nu}{(1-\alpha)nF} \quad (2)$$

$$\log k_s = \alpha \log(1-\alpha) + (1-\alpha)\log \alpha - \log\left(\frac{RT}{nF\nu}\right) - \frac{\alpha(1-\alpha)nF\,\Delta E_p}{2.3RT} \quad (3)$$

where E_{pa} and E_{pc} are the oxidation and reduction peak potentials, respectively, n is the number of electron, F is the Faraday constant (96485 C mol^{-1}), R the universal gas constant, T is kelvin temperature. As we can see from the insets b of Figure 6A and Figure 6B, both E_{pa} and E_{pc} are linearly dependent on ln ν with the linear equations of E_{pc}/V = −0.0192 ln ν (V s^{-1}) − 0.0791 (r = 0.9974) and E_{pa}/V = 0.0233 ln ν (V s^{-1}) + 0.1694 (r = 0.9920) for HQ, and E_{pc}/V = −0.0184 ln ν (V s^{-1}) + 0.0382 (r = 0.9992) and E_{pa}/V = 0.0208 ln ν (V s^{-1}) + 0.2595 (r = 0.9920) for CT. Thus, the values of α and k_s were calculated to be 0.55, 0.52 s^{-1} and 0.53, 0.54 s^{-1} for HQ and CT, respectively. All these k_s values are more comparable with those obtain from CdS/r-GO,[11] graphene−chitosan[44] based sensors, suggesting that the DBIs have fast electron transfer kinetics on the developed sensing interface.

For the irreversible oxidation process of RS at $Cu_3(btc)_2$/CS−ERGO/GCE, the following eq 4 was applied:[43]

$$E_{pa} = E^{0'} - \left(\frac{RT}{\alpha nF}\right)\ln\left(\frac{RTk_s}{\alpha nF}\right) + \left(\frac{RT}{anF}\right)\ln \nu \quad (4)$$

where $E^{0'}$ is the formal potential and the meanings of the other symbols are the same as for eqs 1−3). From the relationship of E_{pa} versus ν as shown in Figure S2 in Supporting Information, the value of $E^{0'}$ is estimated to be 0.55 V via extension of the curve to ν = 0. Then from the plot of E_{pa} versus ln ν as displayed in inset b of Figure 6C, the linear regression equation of E_{pa}/V = 0.0307 ln ν (V s^{-1}) + 0.6963 (r = 0.9912) was obtained. Thus, according to slope and intercept of regression equation, the values of α and k_s were calculated to be 0.44 and 0.28 s^{-1}, respectively.

The electrocatalytic rate constants of HQ, CT, and RS at $Cu_3(btc)_2$/CS−ERGO/GCE were further determined by chronoamperometry (CA) tests. Figure 7A-a shows the CA response of 25 mM PBS in the absence and presence of increasing concentrations of HQ at $Cu_3(btc)_2$/CS−ERGO/GCE. Clearly, upon addition of increasing amounts of HQ into

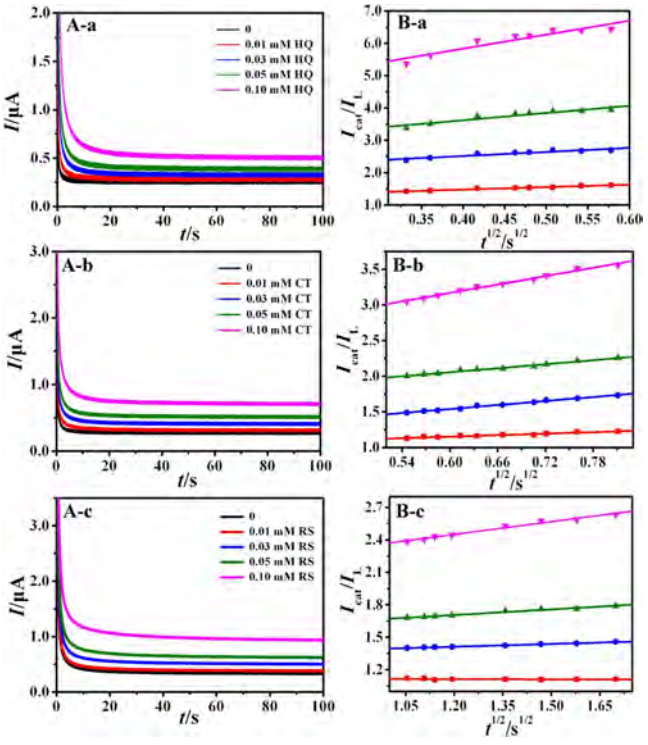

Figure 7. (A) Chronoamperograms of $Cu_3(btc)_2$/CS−ERGO/GCE in 25 mM PBS (pH 7.0) upon adding increasing amounts of HQ (a), CT (b), and RS (c). (B) Plots of I_{cat}/I_L versus $t^{1/2}$.

DOI: 10.1021/acs.jpcc.6b01574
J. Phys. Chem. C 2016, 120, 9794−9803

the supporting electrolyte, the currents increase accordingly, confirming that the sensing layer of $Cu_3(btc)_2$/CS−ERGO has the electrocatalytic effect toward HQ. Then the catalytic rate constant (K_{cat}) of the sensing film toward the HQ was calculated according to the following eq 5:[45]

$$\frac{I_{cat}}{I_L} = (\pi K_{cat} C_0 t)^{1/2} \quad (5)$$

where I_L and I_{cat} are the current of $Cu_3(btc)_2$/CS−ERGO/GCE in the absence and presence of HQ, C_0 is the HQ concentration, and t is the time elapsed. From the data of Figure 7A-a, the relationship of I_{cat}/I_L versus $t^{1/2}$ at different concentrations of DBIs is plotted as Figure 7B-a. Thus, based on the average value of the slopes, the value of K_{cat} for the sensor to HQ is obtained to be 3.2×10^5 M^{-1} s^{-1}. Figure 7A-b and Figure 7A-c show the CA curves of CT (b) and RS (c) at $Cu_3(btc)_2$/CS−ERGO/GCE, and the corresponding linear relationships of I_{cat}/I_L versus $t^{1/2}$ are displayed in Figure 7B-b and Figure 7B-c. Likewise, the values of K_{cat} for CT and RS were calculated to be 7.8×10^4 M^{-1} s^{-1} and 1.9×10^3 M^{-1} s^{-1}, respectively. The results demonstrate that the $Cu_3(btc)_2$/CS−ERGO has excellent catalytic activity toward HQ, CT, and RS, which is likely induced by the favorable electron transfer and abundant active site of $Cu_3(btc)_2$/CS−ERGO.

3.6. Simultaneous Determination of DBIs. DPV technology possesses higher sensitivity and better resolution than CV technique for quantitative analysis because it is achieved by applying a small voltage pulse superimposed on the linear voltage sweep and sampling the differential current at a short time after the pulse.[46] So the DPV was further utilized to evaluate the performance of the $Cu_3(btc)_2$/CS−ERGO-based sensor for the quantitative analysis of HQ, CT, and RS. Figure 8A shows the DPVs of 30 μM CT and 30 μM RS with increasing amounts of HQ at $Cu_3(btc)_2$/CS−ERGO/GCE. Obviously, the peaks of CT and RS are hardly changed throughout the tests, which suggests that their oxidation products do not irreversibly adsorb on the surface of $Cu_3(btc)_2$/CS−ERGO/GCE to hinder the detection of the others. But the oxidation peaks of HQ enhanced gradually with the increase of HQ concentrations, and the oxidation peak currents (I_{pa}) show a good linear relationship with the concentrations of HQ (C_{HQ}) over the range from 5.0 to 400 μM (inset of Figure 8A), with the regression equation of $I_{pa}/\mu A = -0.0168C_{HQ}$ (μM) − 0.3052 (r = 0.9939). Then based on signal-to-noise (S/N = 3) characteristic, the limit of detection (LOD) was estimated to be 0.44 μM. Similarly, keeping the concentrations of HQ and RS at 30 μM in 25 mM PBS (pH 7.0), the peak currents (I_{pa}) of CT show a good linear relationship with CT concentrations in the range from 2.0 to 200 μM (Figure 8B), with the linear equation of $I_{pa}/\mu A = -0.0687C_{CT}$ (μM) − 0.0506 (r = 0.9992) (inset of Figure 8B). Also when S/N = 3, the LOD of CT was estimated to be 0.41 μM. Figure 8C shows DPVs of different concentration of RS in 25 mM PBS (pH 7.0) coexisting with 30 μM HQ and CT. The result shows that I_{pa} is proportional to the concentration of RS in the range from 1.0 μM to 200 μM. The regression equation is $I_{pa}/\mu A = -0.0803C_{RS}$ (μM) − 0.0213 (r = 0.9965) (inset of Figure 8C), and the LOD was calculated to be 0.33 μM (S/N = 3). All these assays indicate that the proposed sensor allows the simultaneous and sensitive detection of HQ, CT, and RS without interference from each other.

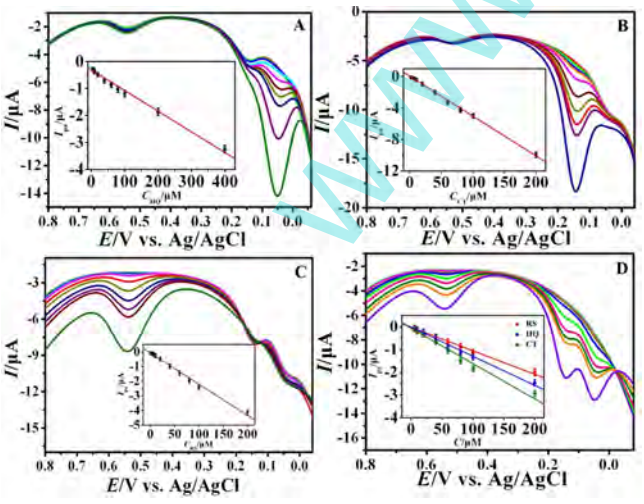

Figure 8. DPVs of $Cu_3(btc)_2$/CS−ERGO/GCE in 25 mM PBS (pH 7.0) containing a mixture of DBIs. A: 30 μM CT, 30 μM RS, 5.0−400 μM HQ. B: 30 μM HQ, 30 μM RS, 2.0−200 μM CT. C: 30 μM HQ, 30 μM CT, 1.0−200 μM RS. D: 5.0−200 μM HQ, CT, and RS. Insets show the relationship of I_{pa} versus the concentrations of DBIs.

Furthermore, the $Cu_3(btc)_2$/CS−ERGO/GCE was applied for the simultaneous determination of HQ, CT, and RS, in which the concentrations of HQ, CT, and RS are changed simultaneously. As shown in Figure 8D, three well-distinguished oxidation peaks are observed, indicating that the catalytic reactions of HQ, CT, and RS at $Cu_3(btc)_2$/CS−ERGO/GCE occur independently. The oxidation peak currents (I_{pa}) of HQ, CT, and RS increase linearly with their concentrations in the ranges from 5.0 μM to 200 μM. The regression equations are $I_{pa}/\mu A = -0.0128C_{HQ}$ (μM) − 0.3188 (r = 0.9954) for HQ, $I_{pa}/\mu A = -0.0556C_{CT}$ (μM) − 0.0643 (r = 0.9917) for CT, and $I_{pa}/\mu A = -0.0203C_{RS}$ (μM) − 0.0841 (r = 0.9974) for RS. Thus, the results demonstrate that HQ, CT, and RS can be selectively determined by $Cu_3(btc)_2$/CS−ERGO/GCE without interference from each other. Table S1 in Supporting Information shows the comparison of analytical performance of DBIs at $Cu_3(btc)_2$/CS−ERGO/GCE and that at the other sensors, from which we can see that our $Cu_3(btc)_2$/CS−ERGO based sensor has comparable and even better performance for the detection of DBIs. This also demonstrates that the sensor holds great application prospect for simultaneous determination of the DBIs.

3.7. Interference Studies. One important issue for the feasibility of a sensor is its capability to distinguish the analytes from interferents. In this work, the electrochemical responses of 50 μM HQ, CT, and RS were measured at $Cu_3(btc)_2$/CS−ERGO/GCE in the presence of different interferents. The results show that the common inorganic ions such as K^+, Na^+, Ca^{2+}, Mg^{2+}, Zn^{2+}, Cl^-, NO_3^-, and SO_4^{2-} in 100-fold excess do not show interference to HQ, CT, and RS detection (signal change below 5%). In addition, the effects of some organic and biological molecules (10-fold excess) such as 2-nitrophenol, 4-nitrophenol, glycine, urea acid, glucose, ascorbic acid, citric acid, methylparaben, *p*-aminophenol, acetone on electrochemical response of DBIs were also investigated, and all the response variations are lower than 7.5%. All these results suggest that the sensor has a satisfactory anti-interference ability for determination of HQ, CT, and RS.

3.8. Reproducibility and Stability. The reproducibility of $Cu_3(btc)_2$/CS−ERGO/GCE was evaluated by preparing five parallel electrodes for the determination of 0.1 mM HQ, CT,

DOI: 10.1021/acs.jpcc.6b01574
J. Phys. Chem. C 2016, 120, 9794−9803

and RS. The relative standard deviations (RSDs) of the five electrodes are 3.4%, 4.1%, and 3.9% for HQ, CT, and RS, respectively. The stability of the modified electrode was also investigated. After the modified electrode was kept at ambient temperature for 2 weeks, repeatable sensing performance was achieved for detection of HQ, CT, and RS, suggesting that the sensor has good stability.

3.9. Real Sample Analysis. Real-time monitoring performance of the fabricated sensor was checked by detecting HQ, CT, and RS in different real environmental water samples. The results are shown in Table S2 in Supporting Information. The recoveries are in range of 98.0−101.4%, suggesting good feasibility and reliability of the proposed electrode for simultaneous detection of HQ, CT, and RS in water samples.

4. CONCLUSION

On the basis of the good electrochemical activity, high specific surface areas, and excellent flexibility of the pore size/wall modification, MOFs receive increasing attention in the electrochemical sensing field. However, the application of MOFs as sensing materials for the simultaneous detection of isomers has not been reported yet. In this work, an electroactive MOF of $Cu_3(btc)_2$ covalently immobilized at the CS−rGO film was applied as a sensing interface for the simultaneous determination of DBIs of catechol (CT), resorcinol (RS), and hydroquinone (HQ). The results show that based on the unique structure of $Cu_3(btc)_2$, the DBIs of RS, CT, HQ can well be separated from each other with a large peak potential difference. Meanwhile, the high conductivity of the CS−ERGO matrix greatly enhances the electrochemical signal intensity of the DBIs, leading to high sensitivities of sensor toward the DBIs. Also the satisfactory results are obtained for the determination of the DBIs in the real samples by the prepared sensor, which broadens the application of the MOF materials in the analytical fields.

■ ASSOCIATED CONTENT

Supporting Information

The Supporting Information is available free of charge on the ACS Publications website at DOI: 10.1021/acs.jpcc.6b01574.

Effect of oxygen on the CVs of CS−GO/GCE (Figure S1); plot of peak potential versus the scan rate for RS (Figure S2); flat band model and quantum chemical calculation (Figure S3); comparison of the sensing characteristics (Table S1); analytical results for real water samples (Table S2) (PDF)

■ AUTHOR INFORMATION

Corresponding Author

*E-mail: axiang236@126.com. Phone: +86-596-2591445. Fax: +86-596-2520035.

Notes

The authors declare no competing financial interest.

■ ACKNOWLEDGMENTS

The work is supported by the National Natural Science Foundation of China (Grant 21275127) and Key Research Foundation of Fujian Education Department (Grant JA14195, JA15305).

■ REFERENCES

(1) Perry, D. A.; Razer, T. M.; Primm, K. M.; Chen, T. Y.; Shamburger, J. B.; Golden, J. W.; Owen, A. R.; Price, A. S.; Borchers, R. L.; Parker, W. R. Surface-Enhanced Infrared Absorption and Density Functional Theory Study of Dihydroxybenzene Isomer Adsorption on Silver Nanostructures. *J. Phys. Chem. C* **2013**, *117*, 8170−8179.

(2) Becerra-Herrera, M.; Sánchez-Astudillo, M.; Beltrán, R.; Sayago, A. Determination of phenolic compounds in olive oil: New Method Based on Liquid-Liquid Micro Extraction and Ultra High Performance Liquid Chromatography-Triple-Quadrupole Mass Spectrometry. *LWT-Food Sci. Technol.* **2014**, *57*, 49−57.

(3) Li, Y.; Huang, H.; Ma, Y.; Tong, J. Highly Sensitive Fluorescent Detection of Dihydroxybenzene Based on Graphene Quantum Dots. *Sens. Actuators, B* **2014**, *205*, 227−233.

(4) Lu, Q.; Hu, H.; Wu, Y.; Chen, S.; Yuan, D.; Yuan, R. An Electrogenerated Chemiluminescence Sensor Based on Gold Nanoparticles@C_{60} Hybrid for the Determination of Phenolic Compounds. *Biosens. Bioelectron.* **2014**, *60*, 325−331.

(5) Nagaraja, P.; Vasantha, R. A.; Sunitha, K. R. A Sensitive and Selective Spectrophotometric Estimation of Catechol Derivatives in Pharmaceutical Preparations. *Talanta* **2001**, *55*, 1039−1046.

(6) Liao, C. L.; Ku, K. L. Development of a Signal-Ratio-Based Antioxidant Index for Assisting the Identification of Polyphenolic Compounds by Mass Spectrometry. *Anal. Chem.* **2012**, *84*, 7440−7448.

(7) He, J.; Yao, F.; Cui, H.; Li, X.; Yuan, Z. Simultaneous Determination of Dihydroxybenzene Positional Isomers by Capillary Electrochromatography Using Gold Nanoparticles as Stationary Phase. *J. Sep. Sci.* **2012**, *35*, 1003−1009.

(8) Medina-Plaza, C.; Rodriguez-Mendez, M. L.; Sutter, P.; Tong, X.; Sutter, E. Nanoscale Au-In Alloy-Oxide Core-Shell Particles as Electrocatalysts for Efficient Hydroquinone Detection. *J. Phys. Chem. C* **2015**, *119*, 25100−25107.

(9) Ahammad, A. J. S.; Rahman, M. M.; Xu, G. R.; Kim, S.; Lee, J. J. Highly Sensitive and Simultaneous Determination of Hydroquinone and Catechol at Poly(thonine) Modified Glassy Carbon Electrode. *Electrochim. Acta* **2011**, *56*, 5266−5271.

(10) Wang, Z.; Li, S.; Lv, Q. Simultaneous Determination of Dihydroxybenzene Isomers at Single-wall Carbon Nanotube Electrode. *Sens. Actuators, B* **2007**, *127*, 420−425.

(11) Hu, S.; Zhang, W.; Zheng, J.; Shi, J.; Lin, Z.; Zhong, L.; Cai, G.; Wei, C.; Zhang, H.; Hao, A. One Step Synthesis Cadmium Sulphide/Reduced Graphene Oxide Sandwiched Film Modified Electrode for Simultaneous Electrochemical Determination of Hydroquinone, Catechol and Resorcinol. *RSC Adv.* **2015**, *5*, 18615−18621.

(12) Wang, H.; Wu, Y.; Yan, X. Room-Temperature Phosphorescent Discrimination of Catechol from Resorcinol and Hydroquinone Based on Sodium Tripolyphosphate Capped Mn-Doped ZnS Quantum Dots. *Anal. Chem.* **2013**, *85*, 1920−1925.

(13) Zhou, X.; He, Z.; Lian, Q.; Li, Z.; Jiang, H.; Lu, X. Simultaneous Determination of Dihydroxybenzene Isomers Based on Graphene-Graphene Oxide Nanocomposite Modified Glassy Carbon Electrode. *Sens. Actuators, B* **2014**, *193*, 198−204.

(14) Chen, Z.; Adil, K.; Weselinski, Ł. J.; Belmabkhout, Y.; Eddaoudi, M. A Supermolecular Building Layer Approach for Gas Separation and Storage Applications: the Eea and rtl-MOF Platforms for CO_2 Capture and Hydrocarbon Separation. *J. Mater. Chem. A* **2015**, *3*, 6276−6281.

(15) Li, L.; Tang, S.; Wang, C.; Lv, X.; Jiang, M.; Wu, H.; Zhao, X. High Gas Storage Capacities and Stepwise Adsorption in a UiO Type Metal-Organic Framework Incorporating Lewis Basic Bipyridyl Sites. *Chem. Commun.* **2014**, *50*, 2304−2307.

(16) Na, K.; Choi, K. M.; Yaghi, O. M.; Somorjai, G. A. Metal Nanocrystals Embedded in Single Nanocrystals of MOFs Give Unusual Selectivity as Heterogeneous Catalysts. *Nano Lett.* **2014**, *14*, 5979−5983.

(17) He, Y.; Xiang, S.; Zhang, Z.; Xiong, S.; Fronczek, F. R.; Krishna, R.; O'Keeffe, M.; Chen, B. A Microporous Lanthanide-Tricarboxylate

DOI: 10.1021/acs.jpcc.6b01574
J. Phys. Chem. C 2016, 120, 9794−9803

Framework with the Potential for Purification of Natural Gas. *Chem. Commun.* **2012**, *48*, 10856−10858.
(18) Proietti, E.; Jaouen, F.; Lefèvre, M.; Larouche, N.; Tian, J.; Herranz, J.; Dodelet, J. P. Iron-Based Cathode Catalyst with Enhanced Power Density in Polymer Electrolyte Membrane Fuel Cells. *Nat. Commun.* **2011**, *2*, 416.
(19) Choi, K. M.; Jeong, H. M.; Park, J. H.; Zhang, Y. B.; Kang, J. K.; Yaghi, O. M. Supercapacitors of Nanocrystalline Metal-Organic Frameworks. *ACS Nano* **2014**, *8*, 7451−7457.
(20) Li, Y.; Pang, A.; Wang, C.; Wei, M. Metal-Organic Frameworks: Promising Materials for Improving the Open Circuit Voltage of Dye-Sensitized Solar Cells. *J. Mater. Chem.* **2011**, *21*, 17259−17264.
(21) Combelles, C.; Yahia, M. B.; Pedesseau, L.; Doublet, M.-L. Design of Electrode Materials for Lithium-Ion Batteries: The Example of Metal-Organic Frameworks. *J. Phys. Chem. C* **2010**, *114*, 9518−9527.
(22) Ling, P.; Lei, J.; Zhang, L.; Ju, H. Porphyrin-Encapsulated Metal-Organic Frameworks as Mimetic Catalysts for Electrochemical DNA Sensing via Allosteric Switch of Hairpin DNA. *Anal. Chem.* **2015**, *87*, 3957−3963.
(23) Xu, Z.; Yang, L.; Xu, C. Pt@UiO-66 Heterostructures for Highly Selective Detection of Hydrogen Peroxide with an Extended Linear Range. *Anal. Chem.* **2015**, *87*, 3438−3444.
(24) Fernandes, D. M.; Barbosa, A. D. S.; Pires, J.; Balula, S. S.; Cunha-Silva, L.; Freire, C. Novel Composite Material Polyoxovanadate@MIL-101(Cr): A Highly Efficient Electrocatalyst for Ascorbic Acid Oxidation. *ACS Appl. Mater. Interfaces* **2013**, *5*, 13382−13390.
(25) Wang, X.; Wang, Q.; Wang, Q.; Gao, F.; Gao, F.; Yang, Y.; Guo, H. Highly Dispersible and Stable Copper Terephthalate Metal-Organic Framework-Graphene Oxide Nanocomposite for an Electrochemical Sensing Application. *ACS Appl. Mater. Interfaces* **2014**, *6*, 11573−11580.
(26) Guo, H.; Zhu, G.; Hewitt, I. J.; Qiu, S. "Twin Copper Source" Growth of Metal-Organic Framework Membrane: $Cu_3(BTC)_2$ with High Permeability and Selectivity for Recycling H_2. *J. Am. Chem. Soc.* **2009**, *131*, 1646−1647.
(27) Liu, Y.; Zhang, Y.; Chen, J.; Pang, H. Copper metal-organic framework nanocrystal for plane effect nonenzymatic electro-catalytic activity of glucose. *Nanoscale* **2014**, *6*, 10989−10994.
(28) Wang, Y.; Wu, Y.; Xie, J.; Ge, H.; Hu, X. Multi-Walled Carbon Nanotubes and Metal-Organic Framework Nanocomposites as Novel Hybrid Electrode Materials for the Determination of Nano-Molar Levels of Lead in a Lab-on-Valve Format. *Analyst* **2013**, *138*, 5113−5120.
(29) Yang, J.; Zhao, F.; Zeng, B. One-step Synthesis of a Copper-Based Metal-Organic Framework-Graphene Nanocomposite with Enhanced Electrocatalytic Activity. *RSC Adv.* **2015**, *5*, 22060−22065.
(30) Alves, N. M.; Mano, J. F. Chitosan Derivatives Obtained by Chemical Modifications for Biomedical and Environmental Applications. *Int. J. Biol. Macromol.* **2008**, *43*, 401−414.
(31) Rinaudo, M. Chitin and Chitosan: Properties and Applications. *Prog. Polym. Sci.* **2006**, *31*, 603−632.
(32) Hummers, W. S., Jr.; Offeman, R. E. Preparation of Graphitic Oxide. *J. Am. Chem. Soc.* **1958**, *80*, 1339−1339.
(33) Zhang, Y.; Bo, X.; Luhana, C.; Wang, H.; Li, M.; Guo, L. Facile Synthesis of a Cu-Based MOF Confined in Macroporous Carbon Hybrid Material with Enhanced Electrocatalytic Ability. *Chem. Commun.* **2013**, *49*, 6885−6887.
(34) Talin, A. A.; Centrone, A.; Ford, A. C.; Foster, M. E.; Stavila, V.; Haney, P.; Kinney, R. A.; Szalai, V.; Gabaly, F. E.; Yoon, H. P.; et al. Tunable Electrical Conductivity in Metal-Organic Framework Thin-Film Devices. *Science* **2014**, *343*, 66−69.
(35) Frisch, M. J.; Trucks, G. W.; Schlegel, H. B.; Scuseria, G. E.; Robb, M. A.; Cheeseman, J. R. *Guassian 09*, revision A; Guassian Inc.: Wallingford, CT, 2009.
(36) Valiev, M.; Bylaska, E. J.; Govind, N.; Kowalski, K.; Straatsma, T. P.; Van Dam, H. J. J.; Wang, D.; Nieplocha, J.; Apra, E.; Windus, T. L.; et al. NWChem: A Comprehensive and Scalable Open-Source Solution for Large Scale Molecular Simulations. *Comput. Phys. Commun.* **2010**, *181*, 1477−1489.
(37) Becke, A. D. Density-Functional Thermochemistry. III. The Role of Exact Exchange. *J. Chem. Phys.* **1993**, *98*, 5648.
(38) Schäfer, A.; Horn, H.; Ahlrichs, R. Fully Optimized Contracted Gaussian Basis Sets for Atoms Li to Kr. *J. Chem. Phys.* **1992**, *97*, 2571.
(39) Huang, W.; Zhou, X.; Xia, Q.; Peng, J.; Wang, H.; Li, Z. Preparation and Adsorption Performance of GrO@Cu-BTC for Separation of CO_2/CH_4. *Ind. Eng. Chem. Res.* **2014**, *53*, 11176−11184.
(40) Ling, P.; Lei, J.; Zhang, L.; Ju, H. Porphyrin-Encapsulated Meta-Organic Frameworks as Mimetic Catalysts for Electrochemical DNA Sensing via Allosteric Switch of Hairpin DNA. *Anal. Chem.* **2015**, *87*, 3957−3963.
(41) Kumar, A. S.; Sornambikai, S. Selective Amperometric Sensing of Hydrogen Peroxide with Nafion/Copper Particulates Chemically Modified Electrode. *Indian J. Chem.* **2009**, *48*, 940−945.
(42) Yue, H. Y.; Huang, S.; Chang, J.; Heo, C.; Yao, F.; Adhikari, S.; Gunes, F.; Liu, L. C.; Lee, T. H.; Oh, E. S.; et al. ZnO Nanowire Arrays on 3D Hierachical Graphene foam: Biomarker Detection of Parkinson's Disease. *ACS Nano* **2014**, *8*, 1639−1646.
(43) Laviron, E. General Expression of the Linear Potential Sweep Voltammogram in the Case of Diffusionless Electrochemical Systems. *J. Electroanal. Chem. Interfacial Electrochem.* **1979**, *101*, 19−28.
(44) Yin, H.; Zhang, Q.; Zhou, Y.; Ma, Q.; liu, T.; Zhu, L.; Ai, S. Electrochemical Behavior of Catechol, Resorcinol and Hydroquinone at Graphene-Chitosan Composite Film Modified Glassy Carbon Electrode and Ttheir Simultaneous Determination in Water Samples. *Electrochim. Acta* **2011**, *56*, 2748−2753.
(45) Bard, A. J.; Faulkner, L. R. *Electrochemical Methods: Fundamentals and Applications*; Wiley: New York, 2001.
(46) Zhang, Y.; Wang, Y.; Wang, H.; Jiang, J. H.; Shen, G. L.; Yu, R. Q.; Li, J. Electrochemical DNA Biosensor Based on the Proximity-Dependent Surface Hybridization Assay. *Anal. Chem.* **2009**, *81*, 1982−1987.

DOI: 10.1021/acs.jpcc.6b01574
J. Phys. Chem. C 2016, 120, 9794−9803